Compound-Specific Imaging of Methanol Fuel Cell for Performance and Degradation Studies Using a Mini Positron Emission Tomograph

Eva Sarkadi-Priboczki,* Mate Varga, Ivan Valastyan, Karoly Brezovcsik, Andras Fenyvesi, and Jozsef Molnar[a]

Direct methanol fuel cell is a promising electrical energy source. Performance improvements, such as higher energy density and improved electrocatalyst are hot topics in fuel cell research. The goal of this study is the introduction of the Positron Emission Tomography (PET) as molecular imaging technique in the visualization of the methanol fuel cell process. The compound specific imaging method, using a small PET camera and radiolabeled ^{11}C methanol, can visualize the electrocatalytic processes, the coverage degree and the distribution of the methanol and its derivatives on the total electrocatalyst surface. The undesirable methanol crossover effect was also detected by imaging the additional layers of the cell. The fuel cell layers were studied in different conditions, such as well-functioning and temporarily or permanently degraded, during short- and long-term operations. The experimental results confirmed the PET imaging method is applicable in the methanol fuel cell development.

1. Introduction

Fuel cell is one of the possible sources of electrical energy. Within the methanol fuel cell (research work of G. Olah in 1990s) types, the direct methanol fuel cell is a proton-exchange fuel cell directly using methanol-water solution as fuel without methanol to hydrogen transformation unit.[1] The liquid methanol fuel cell, thanks to its high theoretical energy density, simple structure without thermal management and easy storage and transportation, is more suitable for our purpose than the hydrogen gas fuel cell. The methanol fuel cell is a promising electrical energy source used in laptops, mobile phones, digital cameras etc. However, there are several unsolved problems in its effective operation which limit its widespread use. The disadvantage of methanol fuel cell operation is particularly the temporary and the permanent degradations of the catalysts which make the cell a lower–power density in practice.[2–5] The temporary or recoverable degradation (CO_2 accumulation at the anode, the cathode water flooding etc.) is recovered after stopping the operation but the permanent or irrecoverable degradation remains the next time they are used.

In addition to the catalysts quality, the diffusion layers, the membrane and the cell energy efficiency also depend on the operating conditions like the methanol concentration, the temperature, the oxygen pressure and the number of cells.[6–15] The current work was performed using a simple commercial Direct Methanol Fuel Cell (DMFC) involving one cell with simple air window (air breath for oxygen uptake) and single methanol-water solution uploading (without fuel flow) at room temperature.[16] The cell itself consists of the anode and the cathode perforated current collector plates with circular holes placed in a square grid and between them, the MEA (Membrane Electrode Assembly) with a multi-layer structure. The MEA as the DMFC key component consists of two very thin porous hydrophobic gas diffusion layers (retaining the water passage from the methanol aqueous solution), the anode and the cathode catalyst layers and, in the middle, the proton-exchange membrane layer. The Pt/Ru anode catalyst is responsible for methanol electro-oxidation while the hydrogen oxidation process (using airgaps for oxygen supply from air) takes place on a Pt cathode catalyst.[17] The Nafion proton-exchange membrane conducts hydrogen ions from the anode to the cathode catalyst.

The electrocatalytic processes take place on the anode and on the cathode catalyst surfaces. The first step of the methanol electro-oxidation is the methanol adsorption and dissociation on the Pt anode layer, followed by CO_{ads} decomposing and/or formyl-like species-CHO_{ads}.[18–22] Since the CO-poisoned species can be formed on pure Pt electrocatalyst thus the alloy of Pt with Ru is applied for decreasing of the poison surface. The water dissociates to OH_{ads} and adsorbed on Ru sites. The CO and OH adsorbed species form together to CO_2 final product on the anode catalyst. One of the further research purposes is to find the best Pt–M alloy anode for an efficient cell.[23–24] The current work contributes to the profiling and monitoring of the electrocatalyst processes inside the MEA region during the DMFC processes. Considering the cathode catalyst, the catalytic

[a] Dr. E. Sarkadi-Priboczki, M. Varga, Dr. I. Valastyan, K. Brezovcsik, Dr. A. Fenyvesi, Dr. J. Molnar
Institute for Nuclear Research
4026 Debrecen
Bem square 18/c (Hungary)
E-mail: priboczki.eva@atomki.hu

oxidation of the hydrogen ion (the hydrogen ion itself formed originally at the anode side) to water is not radiolabeled reaction. Nevertheless, if some radioactivity can be visualized by PET in the cathode region, it may refer to undesired crossover effects of ^{11}C-methanol. This way the PET is an additional method for crossover effect detection. A reason of the insufficient DMFC performance is the crossover effect when a part of the methanol (and carbon dioxide) pass through the membrane to the cathode area.[25] This reduces the cathode potential thereby the overall voltage of the cell.

Herein a DMFC education product (Heliocentris GmbH, catalysts made of mixed metal, PtRu/C and Pt/C catalytic layers on carbon supports) was applied with circa 10% efficiency for demonstration of the PET imaging capability and applicability.[26–29] Although this DMFC cell has low efficiency (usually used just for demonstration) the performance change, methanol accumulation degree and absence can be followed very well. The distributions of the adsorbates (methanol and its derivatives), the possible poison areas and the crossover effect were studied in both of the anode and the cathode catalysts regions. Additionally, two different methanol concentrations were used for the comparison of the adsorbates degrees in the anode catalyst regions.

Several imaging methods are well known for characterization of different processes of physicochemical and electrochemical surface area such as X-ray computed tomography for failure analysis of cell electrode, MRI and Neutron Imaging for water imaging in cell.[30–32] Furthermore different vibrational and fluorescence chemical imaging and electrochemical microscopy methods are also known in adsorption studies.[33–34] The positron emission tomography presented here, a well-known technique for biochemical functional imaging in human and animal bodies, is especially adaptable for profiling and monitoring of positron-emitter labeled compounds in chemically reactive surface area in few cm-scale. The main advantages of positron emission tomography are the high sensitivity and the high molecule specificity. The small detector ring (MiniPET) camera (also known as small animal PET camera) is applied for imaging of the positron-emitter labeled compounds with high ~1.2 mm spatial resolution compared to bigger, human PET camera with 4–5 mm resolution.[35] In the previous works the PET imaging was already effectively used in molecular imaging of liquid chromatography and heterogeneous catalysis processes.[36–38] In the present work the ^{11}C-radiolabeled methanol as a tracing fuel compound (labeled by ^{11}C-positron-emitter isotope) and its ^{11}C-derivatives (their collective name ^{11}C-adsorbates) were determined in terms of chemical property on the reactive surface area along the layers of the fuel cell. Primarily the well-functioning and the gradually degraded anode catalyst was monitored. During the PET imaging the fuel cell was connected to a voltmeter for following the voltage changes during the different cell operations. The linear rainbow color-coding represents the radioactivity concentration degree, i.e. the concentrations of the methanol fuel and its derivatives in the anode and cathode layer regions inside the MEA and in the total cell.

2. Results and discussion

During the experiments the primary goal was the molecular-specific profiling and monitoring of the reactive surface areas within the MEA (Figure 1A, B) of the fuel cell between two collector plates using the PET imaging method (Figure 2A). Concerning the cell function, the radioactivity surface distribution provides relevant information about ^{11}C-adsorbates accumulation, their realignment by electro-oxidation (known that these compounds are mostly ^{11}C-formaldehyde, ^{11}C-formic acid and ^{11}C-carbon monoxide intermediates) and desorption. These processes take place on the anode catalyst surface area and their PET images refer to the fuel cell efficiency, the defects locations and the performance decrease as wear time progresses. Additionally, looking at the cathode area, the PET imaging of the cathode side region profiles the presence and extent of the undesired methanol crossover effect.

2.1. Radioactivity Distribution in the Anode Side Region of MEA

Since the ^{11}C is a short lifetime radioisotope (20 min half-life), several consecutive fuel loading and unloading procedures were required to use with high radioactivity and shorter PET

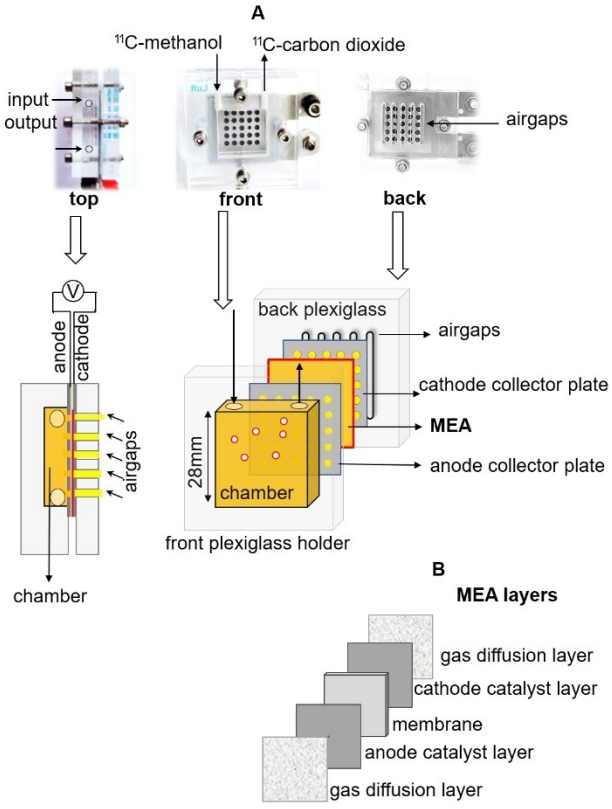

Figure 1. (A) DMFC cell structure: the cell top view with methanol chamber and airgaps units, the cell front view with the ^{11}C-methanol chamber and MEA assembly between two current collector plates and the cell back view with airgaps in the back plexiglass. (B) MEA multi-layer structure.

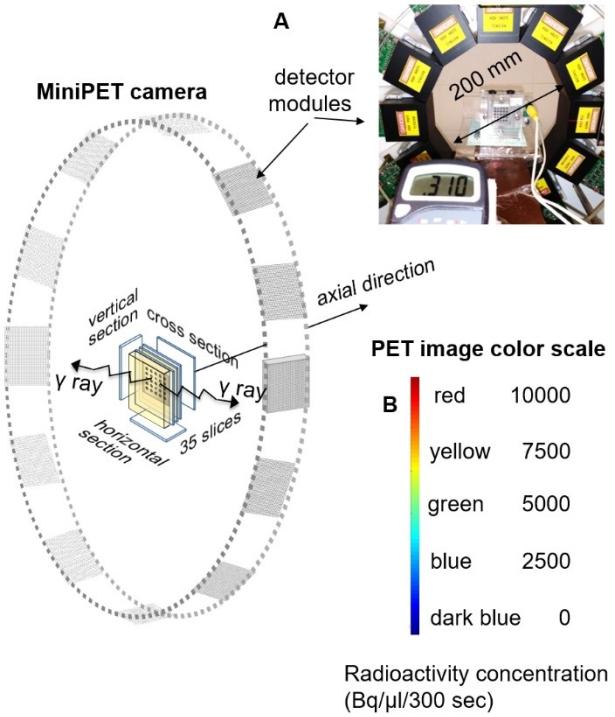

Figure 2. (A) Set up of the DMFC operation inside MiniPET camera: vertical, horizontal and cross sectional views and a photo of the DMFC cell with a voltmeter. (B) radioactivity concentration, assigned to each image pixel is visualized by color scale.

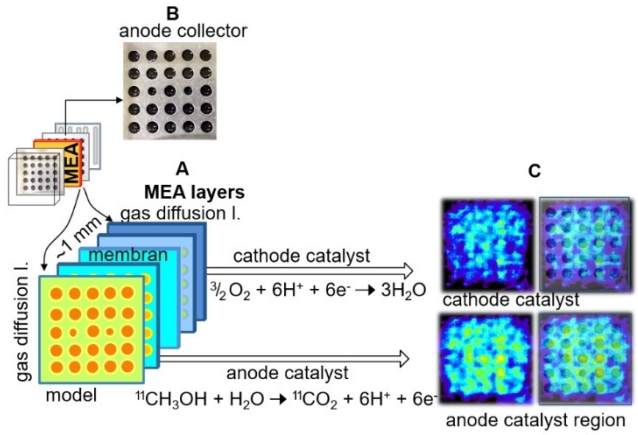

Figure 3. (A) A model of the radioactivity distribution (from yellow to dark blue colors) along the MEA layers. (B) light reflection of the remained radio-methanol solution cover on the holes of the anode collector plate (immediately after emptying the fuel chamber). (C) cross-sectional images of the anode and the cathode catalyst regions with the associated reaction schemes. The perforated collector plate drawing is overlayed in the PET images for easier identification of the radioactive hot spots (images on the right).

data collections instead of a continuous experimental series with a single fuel uploading and unloading.

Following the fuel loading and unloading experimental procedures, at the first step the fuel chamber was filled with ^{11}C-methanol solution. After 5 minutes a PET image was taken about the cell. In the second step the fuel chamber was emptied and thereafter the cell was again PET scanned. This two-step procedure was a required operation in order to achieve high signal-to-background ratios in the PET detectors (here the background was the high radioactive ^{11}C-methanol solution filled in the chamber) thereby getting better quality PET images with sharper contours. This two-step procedure was applicable and useful because the cell voltage level (measured by the voltmeter), i.e. the cell efficiency has not been changed before and after emptying and during this short time operation period (in circa 15—20 minutes of the PET data collections and operations).

Comparing the radioactivity ratios of the filled and the emptied fuel chamber, after emptying the chamber circa 10% of the total radioactivity has remained in the cell and a part of it was just a radioactive methanol solution coverlayer on the anode gas diffusion layer in the anode perforated plate holes. The radioactive methanol solution coverlayer appears as constant and uniform round spots on the PET image (Figure 3A, B, C).

But another part of the radioactivity was accumulated, bounded and/or transformed by electro-oxidation process inside MEA area, mostly on the anode catalyst layer. In terms of the role of the collector plate, some important cell parameters can reduce the performance of the DMFC. One of them is that the methanol passes only through the anode collector holes purely by diffusion (without pump) and the electrocatalysis processes take place especially just on the expanded downstream portions as reactive surface areas (model on Figure 3A). The other of them is that although the catalyst surface size is 20×20 mm, the ^{11}C-methanol can pass only through the holes and gas diffusion layer, after that it can only partially spread on the total catalyst surface (Figure 3C).[39–44]

When this new DMFC cell was operated at the first time, the radioactivity concentrations of the hot spots were comparable along the entire anode catalyst surface areas due to the fresh reactive catalyst surface. The somewhat lower radioactive areas around the hot spots (ring-like) confirm that only part of the methanol was able to spray in the gas diffusion layers (Figure 3, 5 A). Considering the individual layers, the PET image is a merged image of the anode gas diffusion and catalyst layers. Since these layers were pressed together to circa 1 mm width (made by the factory), so it is nearly comparable to the spatial resolution of the PET camera. But using the image corrections and the reconstruction softwares after the PET data collection, the PET images of the anode and the cathode catalyst surface area with perforated current collector regions (1–1 mm width) can be distinguished well from each other (Figure 3C). Additionally, going forward in time, the non-radioactive drop shapes (dark blue drop shape) refer to some water flooding in the cathode side area.

2.2. Quantitative PET Image Analysis

Two radioactivity profile curves (Figure 4) present the radioactivity concentrations as a function of the catalyst distance

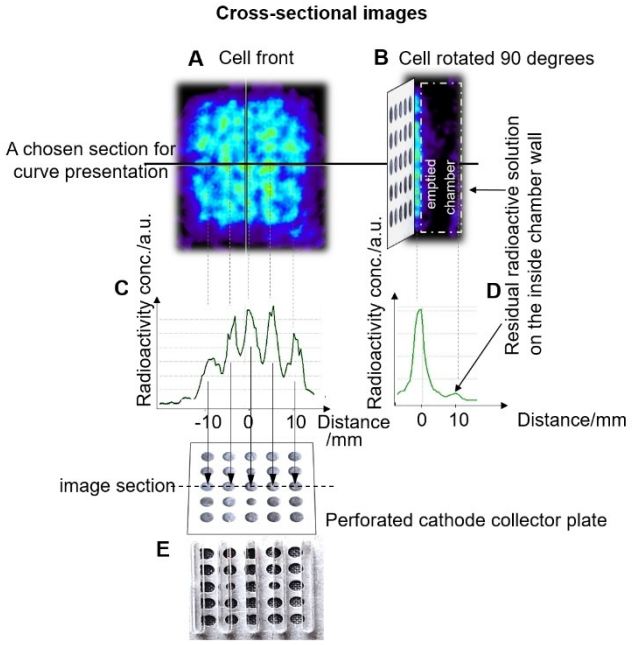

Figure 4. Cross-sectional images of the ^{11}C-adsorbates spatial distribution: (A) PET image of the anode collector side in cell front-view. (B) Cross-sectional image of the cell after cell rotation 90 degrees inside the PET camera (in cell side-view). (C) PET profile curves associated with the PET images of a chosen section (in the middle) on the anode catalyst side area. (D) PET profile curve of the cell side-view. (E) the airgaps left open only partially the holes of the cathode current collector plate.

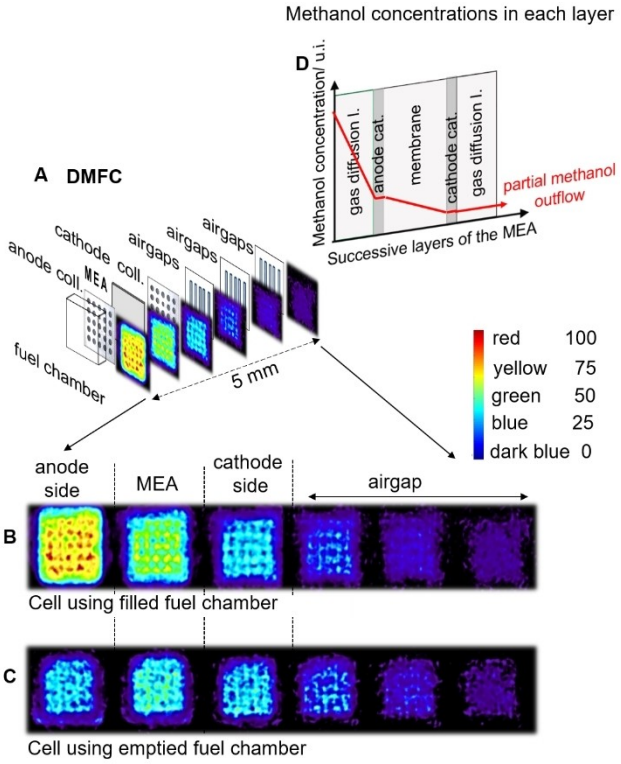

Figure 5. (A) Cross-sectional images of the consecutive slices of MEA multi-layer and current collectors. (B) Enlarged version of the (A) image series with well-defined lattice structure (at filled fuel chamber). (C) Image series after emtying the fuel chamber. (D) A scheme of the methanol concentration profile along the MEA layers.

(the distance along the surface) in the cell front-view, the other curve as a function of the cell thickness in the cell side-view. The 5 separated peaks of the radioactivity concentration profile of a chosen section (Figure 4A, C) of the PET image correspond to the radioactivity spots in the anode region of the MEA (at the emptied chamber). The highest peaks of both curves have the same value due to the chosen section in the middle of the anode surface (Figure 4C, D) while the small peak in the side-view corresponds to a slight radiomethanol solution film remained on the inner wall of the fuel chamber. In both cases the cross-sectional images were chosen here for better image resolution.

The airgaps (for oxygen uptake) behind the cathode current collector plate do not leave all holes open (this geometry made by the factory) (Figure 4E). The airgaps leave the holes fully open only in the middle of the 5 gaps and almost completely closed at the edges. This is an obvious explanation of the radioactivity concentration maximum in the middle and its symmetric, gradual decrease on the right and the left (Figure 4C).

2.3. Undesired Methanol Crossover Effect Penetrating Through Membrane

The red spots on the anode side show the high radioactivity in the first image (Figure 5A, B). The green in the second image, followed the blue areas in the third image show steep decreases in the radioactivity concentration. The radioactivity was the highest in front of the anode gas diffusion layer and then decreased continuously along the anode gas diffusion layer circa to the quarter volume of the initial radioactivity (Figure 5A, B).[45] The radioactivity gradually decreased further along the membrane. This is the methanol crossover, undesired effect because part of the fuel methanol passed through the membrane and the cathode without any useful electro-oxidation reaction. Finally, in the cathode area, circa 5–10% of the initial radioactivity was emitted through airgaps as unconverted methanol.

According to these results the radioactivity concentration rates were on average about one magnitude higher on the anode than on the cathode side.[45] This measurement confirmed the models (Figure 5D) that circa one magnitude change of the methanol concentration occurs within the MEA layers and some methanol can penetrate through the membrane to the cathode catalyst area. Based on the literature mentioned above, this radioactivity is mostly methanol. In the cathode side PET image, the non-radioactive round spots (i.e. deep blue color) can be located referring to the water drops forms (Figure 5B, C).

The methanol crossover effect was further confirmed by PET imaging of some radioactive methanol vapor in the airgaps (Figure 5B, C, last 3 images). The images of 3 orthogonal PET planes showed that part of the methanol was passed through

membrane, the cathode catalyst and the cathode gas diffusion layers and was emitted to airgaps (at the filled chamber, Figure 6). The radioactive vapor between the airgaps is visible in the PET images (Figure 6A) due to the collision of the positron of the ^{11}C-isotope with the plexiglass airgaps walls (the radioactive gas itself is not detectable in low-density air considering the negligible number of positron collisions).

In terms of PET imaging spatial resolution, mostly the cross-sectional images were chosen for presentation of the catalytic processes because the spatial resolution of the cross-sectional image is better compared to the horizontal or the vertical image images due to the square column detector crystals positions (Figure 6). This is the reason why the cell side-view imaging was carried out after the cell was rotated by 90 degree (Figure 4B).

2.4. Anode Catalyst Degradation

The radioactivity degree and distribution i.e. reactive surface coverage rate and its distribution were studied dynamically in the anode catalyst region for a longer time period (several hours). The cell performance has decreased during long usage time (cell voltage has decreased from 0.5 V to 0.3 V). The resulting defects on the catalyst surface may have been created by the ^{11}C-carbon monoxide poison on the anode catalyst and the platinum dissolution and oxidation on the cathode catalyst and these occur as permanent catalyst degradation (irrecoverable). The potential degradation of the very thin gas diffusion layers and the proton-exchange membrane units were not examined separately in this work due to the limited resolution of the MiniPET camera.

At the beginning of the experimental series the PET images showed a representative, quasi-homogeneous radioactivity distribution hot spots on the lattice structure of the anode catalyst surface area. After a certain use, the radioactivity hot spots became quite different during longer usage (10 hours) and more inhomogeneous areas with more local radioactivity absences due to the gradual degradation (Figure 7A). But after the next 10 hours there was somewhat higher radioactivity areas again on the already degraded area (lower right area). A reason could be the partial catalyst recovery (recoverable degradation). During further use, the radioactivity further decreased on the surface, but the special geometric shape of the degraded area (less radioactivity) remained and stabilized, i.e. there was a long-term degradation. It can be concluded, that in long-term application both of temporary and permanent degradations were present.

Continuing the experimental series on the same cell (partially degraded catalyst already) but now using the short-term operation (10-20-30 minutes) the degraded shapes in the PET images have not fundamentally changed, only there were some rearrangement (Figure 7B). These visible modifications presumably were formed by the catalyst's temporary degradation, for example the carbon dioxide as product accumulation

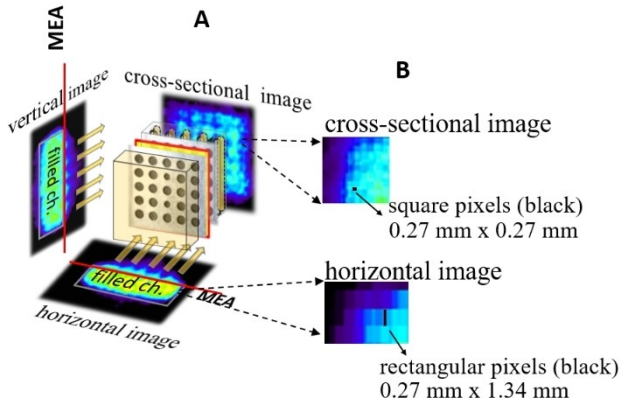

Figure 6. (A) Orthogonal PET imaging schema of the radioactive methanol emission through the cell airgaps. The flow directions are shown by yellow block arrows and the MEA multi-layer position is marked by red lines on the vertical and the horizontal images (filled fuel chamber); the enlarged parts of corresponding cross sectional and horizontal (the same for vertical) pixelated images with their dimensions.

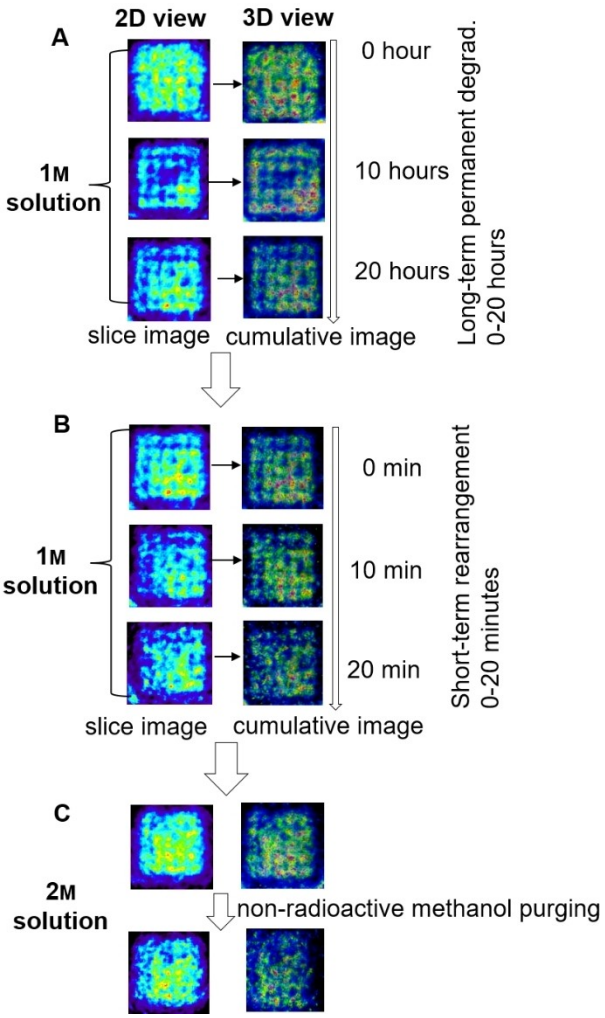

Figure 7. (A) Gradual degradation and defects on the MEA multi-layers during long-term use. The 2D images, the corresponding 3D reconstructed images are presented. (B) The partially degraded cell was used for further short-term measurements. (C) PET images of anode side using 2 M solution and after purging with 2 M non-radioactive methanol solution.

in the fuel that blocked the fuel access to anode catalyst surface or water flooding at cathode as temporary catalyst degradation.

The catalyst degradation degrees are presented in 2D versus 3D (Figure 8) PET images at the same series of measurements (cross-sectional images). The 2D image shows the ^{11}C-adsorbates distribution in a thin slice (1 mm) of the MEA and its close surrounding, while the 3D images show the whole MEA with the current collector plates, even the fuel chamber, as semi-transparent images. When using 2 M methanol solution, the radioactivity degree on the anode surface was higher (Figure 7C) than using 1 M methanol solution (Figure 7B). After non-radioactive methanol purging the radioactivity has equally decreased everywhere on the entire surface, on average the radioactivity decreased by 1/3, but the catalyst defects have remained on the top and left side bars of the surface.

2.5. The 3D Semi-Transparent Image of the Fuel Cell

The whole cell (MEA with current collectors and fuel chamber after emptying the chamber) can be visualized by the PET as a perspective, semi-transparent PET image (3D-reconstructed, multiple slices images of the fuel cell) and shown in Figure 8A, B.

In terms of the degradation imaging, the 3D images show the sum of planar images thus 3D images are more realistic than the 2D representation (Figure 7). The 3D image can be rotated by the processing software.

3. Conclusion

The PET technique is a compound-specific imaging method and it is suitable for profiling and monitoring the methanol electrochemical processes in direct methanol fuel cells. The technology advantage is the methanol fuel and its derivatives can be separated by labeling from other potential or undesirable non-radioactive compounds on the reactive surface. However, the PET imaging method does not give information about what kind of ^{11}C-compounds are accumulated on the radioactive layers. In future the radio-liquid chromatograph and radio-gas chromatograph as additional methods to PET imaging can be perfect for analyzing the ^{11}C-radiolabeled methanol, its ^{11}C-intermediates and ^{11}C-carbon dioxide final product. In the previous work these coupled methods were applied effectively in radiolabeled heterogeneous catalysis investigations.

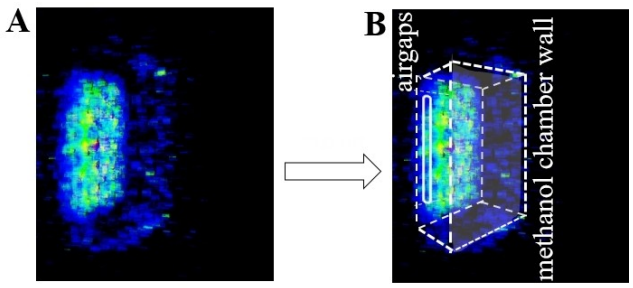

Figure 8. (A) 3D semi-transparent image of an emptied cell and (B) the same image with a cell sketch.

In term of 3D PET imaging, another potential could be the option for visualizing 3–5 or even 10-cell DMFC stack for profiling the radioactivity ratios and the spatial radioactivity distributions along the consecutive MEA layers.

In addition to the methanol, other liquid fuel compounds, such as ethanol, propanol, dimethyl ether and formic acid can be also ^{11}C-radiolabeled for PET imaging as a further research opportunity.

The combined MRI/PET method as an option provides more accurate positioning of the MEA multi-layer by much higher spatial MRI resolution. Moreover, the MRI can be applicable also simultaneously for the water-product detection within the fuel cell.

The PET method has a great perspective for visualizing the radiolabeled fuel compounds and its derivatives on the entire electrochemical surface and it is suitable for developing new catalysts and supports with longer cell lifetime. In future, there is also planned to measure the DMFC polarization curve analyzing more the cell degradation process during PET imaging process. This requires further improvements on the currently operating system.

Experimental Section

Methanol Fuel Radiolabeling

The ^{11}C positron-emitter isotope with 20.4-minute half-life was applied for the methanol tracing. The ^{11}C-methanol was synthesized in a separated radiochemical box and the ^{11}C-methanol gas product was directly trapped in 1 M and, in another series, 2 M non-radioactive methanol-water solution of 6 cm^3. The 6 MBq of the radioactive ^{11}C-methanol solution was portioned for each fuel chamber upload and placed in the center of the field of view of the MiniPET camera. The optimal value of the cell radioactivity was in the range of 0.03–6 MBq considering the PET camera sensitivity, the short half-life radioisotope and the fuel cell size and the geometry. In case of the long-term DMFC processes the ^{11}C-methanol was re-synthetized. The fuel cell was not regenerated after each series of experiments.

PET Camera Parameters

The PET camera detectors are arranged in full ring formation (Figure 2A). The PET camera detects the coincidence of the 511 keV γ rays emitted by the positron-annihilation from the ^{11}C-labeled compounds in the DMFC cell. In this experimental series the voltmeter was used just for the demonstration of the cell work.

The MiniPET is characterized usually with spatial resolution, sensitivity, specificity and field of view. The spatial resolution represents the ability to distinguish two different points after image reconstruction. The sensitivity is defined as the count per unit time of the source activity. It measures how many true coincidence events have been detected for a given source. Since PET detects coincidence events, its sensitivity is very high and only few counts from a beta emitter nuclide are detectable. The sensitivity in the center of the field of view is 6 cps/kBq, measured according to the NEMA NU-4 standard. The specificity means that a selective

compound (here methanol) to be tested will be visible and distinguished from other and undesired compounds in the fuel cell process. The field of view means the spatial dimension at one bed position which can be well imaged by the PET detectors. Objects (here the DMFC) fit in the field of view can be imaged.

The 1–1.2 mm spatial resolution of the MiniPET camera is limited by the crystal size inside the detectors and by the positron range of the ^{11}C radioisotope in different materials. High density materials have shorter positron range and therefore better spatial resolution in the PET images.

The positron range in metals is very short therefore the spatial resolution is limited by the physical size of the scintillation crystals (here 1.27 mm). The average positron range of the ^{11}C isotope in water equivalent compounds is also 1.2 mm which is comparable to the crystal size, therefore in we can use in this case also the crystal size as a measure of the spatial resolution.

The MEA is a thin layer but it has high spatial resolution thanks to its higher density compared to the methanol solution. The cross-sectional images have better resolution with 0.27 mm × 0.27 mm square pixel size, while the vertical and horizontal images have 0.27 mm × 1.34 mm rectangular pixel size due to the crystal size of 1.27 mm × 1.27 mm × 12 mm in the detector module. The commercial Spatiotemporal Modeling Software (used in pre-clinical studies) was applied for planar view image presentation. The 3D image processing software was developed at the institute. Every PET image was calculated from the 35 cross-sectional slices according to the 35 × 35 detector array configuration. The MiniPET camera has a 48 mm high and a 75 mm in diameter cylindrical field of view and the camera maps the samples in 35 cross sectional slices (Figure 2A). The reactive surface size of the MEA is 27 × 27 square mm and the width of the total cell is 16 mm (with plexiglass holders). Usually the fuel cell was projected in the PET images to 15–17 slices with 1.3 mm slice thickness.

The PET color scale quantitatively represents the radioactivity concentrations (Figure 2B) or concentration percentage (Figure 5B, C). The PET data were decay corrected in each experiment.

DMFC Structure

The front transparent plexiglass with the fuel chamber allows the direct observation of the methanol solution with carbon dioxide bubbles (red circles) while in the back plexiglass 5 airgaps provides oxygen supply (Figure 1A). Inside the plexiglass holder, the MEA assembly is placed between two perforated (circular) anode (for methanol passing) and cathode (for air passing) current collector plates. The yellow coloring of some areas indicates the radioactive area (Figure 1A, 2 A).

An image was taken using either 120 second (filled chamber) or 300 second (emptied cell chamber) frame time. The ^{11}C-carbon dioxide gas product itself is invisible inside in the PET image (the gas density is too low for enough detectable positron annihilations). But the bubble wall of radioactive CO_2 could be interfering with radioactive methanol. But the PET data collection was about the emptied fuel cell (anyway, after a while, the CO_2 gas in the methanol solution has already been removed). It can be assumed that if the cell is filled with methanol, the intensive CO_2 gas evolution will be a disturbing effect, even because of the moving CO_2 bubbles during PET data collection.

The cell sizes: collector plates sizes of 27 × 27 mm behind methanol chamber, holes size of 2–3 mm. The anode and the cathode collectors' holes are located opposite to each other. The cell was inserted into the camera in the central position. The bore diameter and depth of the PET camera are 200 mm and 50 mm, respectively.

Since the cross-sectional PET images have better spatial resolution than the horizontal or the vertical sections due to the crystal detector location (Figure 6), therefore the cell was rotated by 90 degrees inside the PET camera in order to sample the MEA layer with higher resolution in a separated experiment (Figure 4B, D).

Acknowledgement

This work was supported by the Economic Development and Innovation Operational Programme (GINOP-2.2.1-15-2016-00012) and it was financed by the Hungarian Government and co-financed by the European Structural Fund.

Conflict of Interest

The authors declare no conflict of interest.

Keywords: catalysis · methanol fuel cells · molecular imaging · performance monitoring · positron emission tomography

[1] S. Surampudi, S. R. Narayanan, E. Vamos, H. Frank, G. Halpert, A. LaConti, J. Kosek, G. K. Surya Prakash, G. A. Olah, *J. Power Sources* **1994**, *47*, 371–385.
[2] A. Casalegno, F. Bresciani, M. Zago, R. Marchesi, *J. Power Sources* **2014**, *249*, 103–109.
[3] A. Bauer, C. W. Oloman, E. L. Gyenge, *J. Power Sources* **2009**, *193*, 754–760.
[4] A. Bashir, N. KingSanders, J.L. Liu, in *Nanostructured Materials for Next-Generation Energy Storage and Conversion, Fuel Cells* (Eds.: F. Li, S. Bashir, J.L. Liu), Springer-Verlag Berlin, **2018**, pp. 1–26.
[5] A. S. Lohoff, D. Günther, M. Hehemann, M. Müller, D. Stolten, *Int. J. Hydrogen Energy* **2016**, *41*, 15325–15334.
[6] P. Kumar, K. Dutta, S. Das, P. P. Kundu, *Int. J. Energy Res.* **2014**, *38*, 1367-1390.
[7] J. G. Liu, T. S. Zhao, R. Chen, C. W. Wong, *Electrochem. Commun.* **2005**, *7*, 288–294.
[8] D. Dixon, K. Wippermannb, J. Mergel, A. Schoekel, S. Zils, C. Roth, *J. Power Sources* **2011**, *196*, 5538–5545.
[9] F. Bresciani, A. Casalegno, J. L. Bonde, M. Odgaard, R. Marchesi, *Int. J. Energy Res.* **2014**, *38*, 117–124.
[10] F. Bresciani, C. Rabissi, A. Casalegno, M. Zago, R. Marchesi, *Int. J. Hydrogen Energy* **2014**, *39*, 21647–21656.
[11] W. Yuan, B. Zhou, J. Hu, J. Deng, Z. Zhang, Y. Tang, *Int. J. Hydrogen Energy* **2015**, *40*, 2326–2333.
[12] Q. Wang, G. Wang, X. Lu, C. Chen, Z. Li, G. Sun, *Int. J. Electrochem. Sci.* **2015**, *10*, 2939–2949.
[13] F. Samimi, M. R. Rahimpour in *Methanol:Science and Engineering* (Eds.:A. Basile, F. Dalena), Elsevier, Amsterdam, **2018**, pp. 381–397.
[14] Y. Na, F. Zenith, U. Krewer, *Energies* **2015**, *8*, 10409–10429.
[15] H. Rivera, J. S. Lawton, D. E. Budil, E. S. Smotkin, *J. Phys. Chem. B* **2008**, *112*, 8542–8548.
[16] N. S. Vasile, A. H. A. M. Videla, S. Specchia, *Chem. Eng. J.* **2017**, *322*, 722–741.
[17] V. B. Silva, A. Rouboa, *Appl. Math. Comput.* **2012**, *218*, 6733–6743.
[18] R. Thimmappa, S. Aralekallu, M.Ch. Devendrachari, A. R. Kottaichamy, Z. M. Bhat, S. P. Shafi, K. S. Lokesh, M. O. Thotiyl, *Adv. Mater. Interfaces* **2017**, *1700321*, 1–7.
[19] E. Antolini, T. Lopes, E. R. Gonzalez, *J. Alloys Compd.* **2008**, *461*, 253–262.
[20] J. Prabhuram, T. S. Zhao, H. Yang, *J. Electroanal. Chem.* **2005**, *578*, 105–112.
[21] V. Raj in *Direct Methanol Fuel Cell Technology* (Ed.: K.Dutta), Elsevier, Amsterdam, **2020**, pp. 495–525.

[22] M. Bayramoglu, Z. Ilbay, *Environ. Prog. Sustain. Energy* **2017**, *36* (6), 1847–1855.
[23] P. Ferrin, A. U. Nilekar, J. Greeley, M. Mavrikakis, J. Rossmeisl, *Surf. Sci.* **2008**, *602*, 3424–3431.
[24] E. Gyenge, in *PEM Fuel Cell Electrocatalysts and Catalyst Layers: Fundamentals and Applications* (Ed.: J. Zhang), Springer-Verlag London **2008**, pp. 165–287.
[25] J. Dinesh, M. Easwaramoorthi, M. Muthukumar, *Int. J.Eng. Trends and Technol.* **2017**, *43*, 5, 284–296.
[26] B. C. Ong, S. K. Kamarudin, S. Basri, *Int. J. Hydrogen Energy* **2017**, *42*, 1014–10157.
[27] S. H. Seo, C. S. Lee, *Appl. Energy* **2010**, *87*, 2597–2604.
[28] O. D. Popovici, M. B.Tataru, F. I. Hathazi, D. M. Popovici, **2015**, *13th International Conference on Engineering of Modern Electric Systems*, EMES, Oradea 2015, pp. 1–4.
[29] O. Popovici, *J. Electr. Electron. Eng., Aust.* **2014**, *7*, 31–34.
[30] S. Mohan, S. O. B. Shrestha, Proceedings of the ASME **2014**, *12th Int. Conf. on Fuel Cell Science, Engineering and Technology, FUELCELL* **2014**, Boston, pp. 1–9.
[31] S. O. B. Shrestha, S. Mohan, *J. Fuel Cell Sci. Technol.* **2014**, *11*, 061009, p. 7.
[32] D. Spernjak, S. G. Advani, A. K. Prasadz, *J. Electrochem.l Soc.* **2009**, *156*, B109–B117.
[33] T. Arlt, A. Schroder, K. Heyne, H. Riesemeier, K. Wippermann, W. Lehnert, I. Manke, *J. Power Sources* **2015**, *297*, 83–89.
[34] Z. Wua, C. S. Wub, P. P. J. Chub, S. Dinga, *Magn. Reson. Imaging* **2009**, *27*, 871–878.
[35] O. Henrotte, T. Bottein, H. Casademont, K. Jaouen, T. Bourgeteau, S. Campidelli, V. Derycke, B. Jousselme, R. Cornut, *ChemPhysChem* **2017**, *18*, 2777–2781.
[36] R. Pini, L. Joss, *Curr. Opin. Chem. Eng.* **2019**, *24*, 37–44.
[37] A. K. Krizsan, I. Lajtos, M. Dahlbom, F. Daver, M. Emri, S. A. Kis, G. Opposits, L. Pohubi, N. Potari, Gy. Hegyesi, G. Kalinka, J. Gal, J. Imrek, F. Nagy, I. Valastyan, B. Kiraly, J. Molnar, D. Sanfilippo, L. Balkay, *J. Nucl. Med.* **2015**, *56*, 1948–1953.
[38] E. Sarkadi-Priboczki, I. Valastyan, J. Molnar, *ChemPlusChem* **2013**, *78*, 830–836.
[39] E. Sarkadi-Priboczki, I. Valastyan, K. Brezovcsik, D. Nagy, G. Opposits, I. Lajtos, M. Emri, L. Balkay, J. Molnar, *ChemistrySelect* **2017**, *2*, 9797–9802.
[40] X. Zhu, N. Kosinov, A. V. Kubarev, A. Bolshakov, B. Mezari, I. Valastyan, J. P. Hofmann, M. B. J. Roeffaers, E. Sarkadi-Priboczki, E. J. M. Hensen, *ChemCatChem* **2017**, *9*, 3470–3477.
[41] Y. Tang, W. Yuan, M. Pan, B. Tang, Z. Li, Z. Wan, *J. Power Sources* **2010**, *195*, 5628–5636.
[42] Y. Q. Xue, H. Guo, H. H. Shang, F. Ye, C. F. Ma, *Energy* **2015**, *81*, 501–510.
[43] L. Wang, Y. Zhang, Y. Zhao, Z. An, Z. Zhou, X. Liu, *J. Micromech. Microeng.* **2011**, *21*, 104012–104021.
[44] Q. Z. Lai, G. P. Yin, Z. B. Wang, *Int. J. Energy Res.* **2009**, *33*, 719–727.
[45] O. A. Obeisun, Q. Meyer, J. Robinson, C. W. Gibbs, A. R. Kucernak, P. R. Shearing, D. J. L. Brett, *Int. J. Hydrogen Energy* **2014**, *39*, 18326–18336.
[46] S. S. Munjewar, S. B. Thombre, R. K. Mallick, *Renewable Sustainable Energy Rev.* **2017**, *67*, 1087–1104.
[47] F. Zenith, U. Krewer, *Energy Environ. Sci.* **2011**, *2*, 519–527.

Manuscript received: November 2, 2020
Version of record online: May 2, 2021